Chapter 4

Nonlinear plant simulator

4.1 Introduction

Figure 3.1 in chapter 3 shows the dependency between the nonlinear models which constitute the mill simulator. In this chapter these dependencies will be studied in earnest with the aim of connecting the models together. Furthermore, the tuning and choice of model constants will be discussed in order to yield realistic simulated behaviour. Plant data obtained from an actual logged Steckel Hot Rolling Mill Process are used as simulator inputs[1].

4.2 Simulator inputs

4.2.1 Introduction

The nonlinear plant simulator is to be used for identifying linear plant models around certain identified operating points. These linear models are highly dependent on the precalculated operating points associated with the generated rolling schedule [18, 59]. The generation of an optimal setup schedule falls outside the scope of this work and a practical schedule was taken as a given input for the simulator. Practical setup schedules were identified from the plant data for the Steckel Hot Rolling Mill process.

In the simulator, only the identified models of chapter 3 are solved and the modelling of the other

[1]It needs to be stressed that the measured plant data has an average time resolution of 0.423 seconds with the mill under closed loop control. This data is helpful, but not completely suited for the tuning of the open loop plant investigated in this study. The open loop data can possibly be extracted from the closed loop results with some added effort, but the impact of this procedure is questionable due to the data's under-sampled nature. It is stated that the hydraulic gauge loop has a bandwidth of 15 Hz [1, 8] which is equivalent to a first order transfer function with a time constant of 10ms, roughly 23 times smaller than the current time resolution of the data.

identified rolling parameters (see figure 3.1) falls outside the scope of this dissertation. Unmodelled parameters (discussed and motivated in section 3.2) that are critical for the functioning of the simulator are:

- The temperature in the roll gap;
- The rolling mill speed;
- Input thickness;
- Rolling schedules.

These modelling deficiencies are compensated for by conditioning real logged plant data for the above variables to be suitable as inputs for the mill simulator.

Operating points were identified from the logged plant data for two similar stainless steel strips of grade 304, which is the most common rolled product of a large stainless steel manufacturer in South Africa[2]. The data show that the strip is usually rolled in a 5-9 pass schedule and that the strip entrance thickness, as obtained from the roughing mill, is about 25mm. In table 4.1 a typical 9 pass rolling schedule is given reflecting entrance and exit thicknesses for each pass. Also shown are the pyrometer measured maximum roll gap entrance and exit temperatures, $\theta_{1_{max}}$ and $\theta_{2_{max}}$ respectively, as well as the measured starting velocity (v_{start}) , threading velocity (v_{thread}) and final velocity (v_{stop}) of the main mill drive.

Table 4.1: Typical Steckel Rolling Mill schedule for the investigated similar strips.

Pass number	$h_1(mm)$	$h_2(mm)$	$\theta^{\circ}_{1_{max}}C$	$\theta^{\circ}_{2_{max}}C$	$v_{start}m.s^{-1}$	$v_{thread}m.s^{-1}$	$v_{stop}m.s^{-1}$
1	25	18.2	980	960	2.1	6	1.8
2	18.2	13.3	967	955	2.1	3.5	1.8
3	13.3	9.7	965	950	2.1	4.8	1.8
4	9.7	7.5	962	948	2.1	6.1	1.8
5	7.5	6.1	957	942	2.1	8	1.8
6	6.1	5.1	955	940	2.1	9.2	1.8
7	5.1	4.3	950	937	2.1	10	1.8
8	4.3	3.7	948	935	2.1	10	1.8
9	3.7	3.3	945	933	2.1	8.5	3.6

The implemented simulator does not have the capability to simulate flatness behaviour of the strip and is only limited to thickness profile simulation. From practical experience[3] [3] the desired thickness profile is rolled during the early passes and during the later passes the flatness (shape) can be controlled. When the strip thickness is greater than 12mm the strip profile is controlled and zero to very

[2]This information was provided by M. Lewis during a personal meeting.

[3]Information supplied by M. Lewis during a personal discussion.

little action can be exerted to control the strip shape/flatness. When the strip thickness falls below 6mm the shape/flatness is controlled and the profile is left unchanged.

4.2.2 Motivation for the choice of simulation operating point

Two rolling schedules and the associated measured data of two similar Stainless Steel grade 304 strips were identified and this data was adapted to form the simulator inputs. It was decided to focus on data of pass 1 and pass 3 in a 5 pass schedule, as possible inputs for the simulator. Some advantages and disadvantages associated with the choice of either of these two passes can be summarized as:

Pass 1:

- If data for pass 1 are used as simulator inputs, the rolling variables might tend to be open loop data and can be used for simulator tuning.
- The possibility exists to perform step tests on the Steckel rolling mill, on which this simulator is based. If this should materialize, defects and disturbances caused by these tests can be corrected for in later passes.
- When pass 1 is chosen as the operating pass, the simulation time interval of the tension model is small and leads to longer computation times.

Pass 3:

- Logged data of pass 3 incorporates effects of control actions taken in previous passes. It might prove difficult to extract open loop data from the available closed loop data. The closed loop logged data can be used to evaluate the performance of the proposed controller against the industrial controller.
- The exit thickness of pass 3 falls on the borderline, where the controllability of profile declines and the controllability of the sheet's shape/flatness increases[4].

Of all of the above points, the computation time was considered to be the most important and weighed heavily in the final choice to make the simulator operable for pass 3.

4.2.3 Rolling variables

The rolling data associated with pass 3 for one of the two identified similar strips were manipulated to serve as input for the mill simulator. In figure 4.1 a measured process speed curve of the main mill drive speed is shown. This batch process exhibits a speed up ramp after tension in the sheet has

[4]Information supplied by M. Lewis during a personal discussion.

been established up to a threading speed. In figure 4.2 the X-ray measured strip input and output thicknesses to and from the roll gap are shown. In figure 4.3 the measured temperatures outside on either side of the roll gap are shown. These temperatures are interpolated linearly in order to obtain a temperature estimate in the roll gap.

The operation point of the simulator was chosen on the mill speed up ramp at a speed of 3.5m/s. This operating point was used, because control is not well addressed on the speed up of the curve [19]. The converse is the norm for the regulation of the rolling process at threading speed [4, 3]. The possible material saving that can result from the elimination of off specification products during the process start and stops can be significant [19].

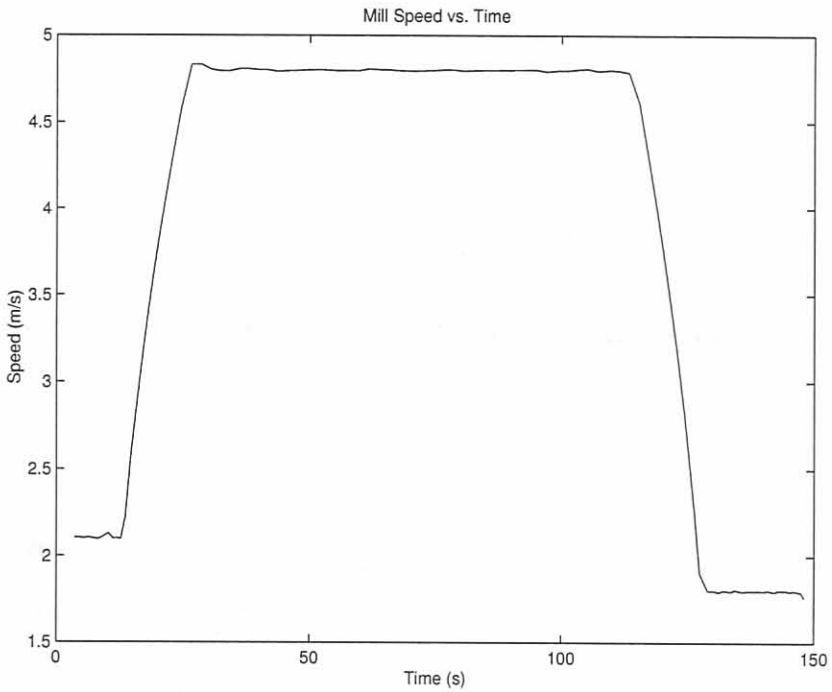

Figure 4.1: Typical speed vs. measured time for pass 3.

4.3 Roll gap model

4.3.1 Solution methodology

The solution of the roll gap model entails the solution of the differential equation model, Eq. 3.15, together with its associated boundary values. Unfortunately the ODE model consists of two independent differential equations on either side of the neutral plane. This phenomenon is due to the frictional forces that work towards the neutral point (see figure 3.2). The general method for solving this model is by numerically integrating the two independent differential equations from either end of the arc of contact while working towards the neutral point of the roll gap.

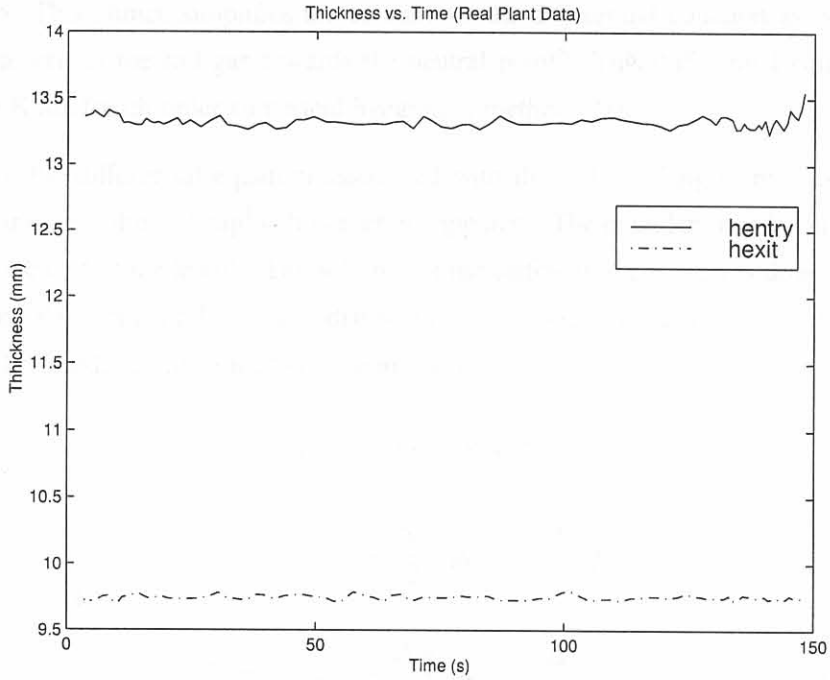

Figure 4.2: Typical entry and exit thicknesses to and from the roll gap vs. the measured time for pass 3.

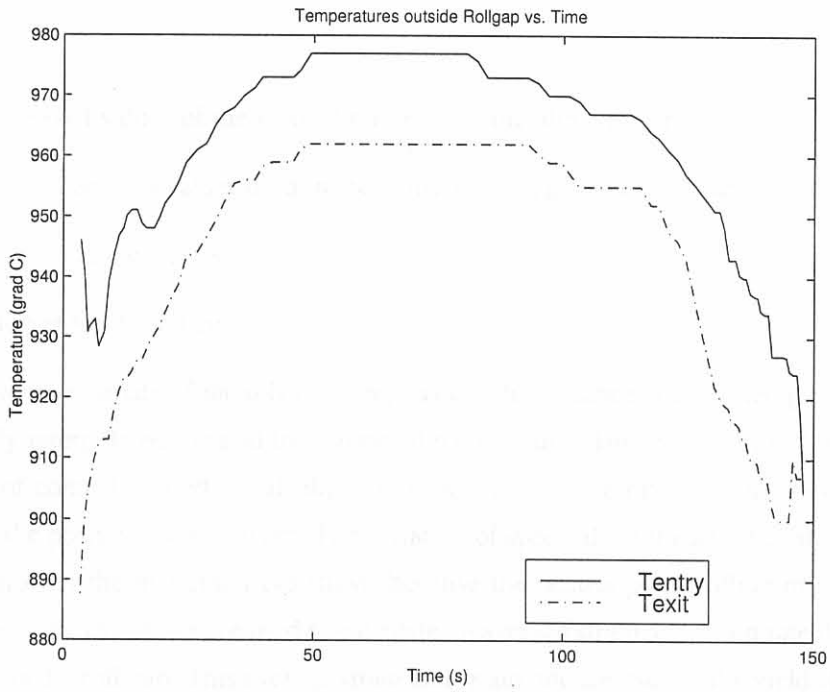

Figure 4.3: Typical entry and exit temperatures to and from the roll gap vs. the measured time for pass 3.

The coordinate system of the roll gap model is chosen such that x_{rg}[5] is increasing towards the entrance of the roll gap. This choice simplifies the solution of the differential equation associated with the length from the exit of the roll gap towards the neutral point[6]. This differential equation is solved using a Runge Kutta fourth order numerical integration method [71].

The solution of the differential equation associated with the roll gap length from the neutral point towards the entrance of the roll gap[7] is however not apparent. The boundary condition of the problem is provided at the end of the length. The solution of the differential equation is done by numerically back-calculating the vertical roll pressure distribution. This back calculation solution is achieved by manipulating the standard Runge Kutta equations as follows:

$$f_1 = f(\phi_{k+1}, p_{k+1}), \tag{4.1}$$

$$f_2 = f(\phi_{k+1} - \frac{\Delta\phi}{2}, p_{k+1} - \frac{\Delta\phi}{2} f_1), \tag{4.2}$$

$$f_3 = f(\phi_{k+1} - \frac{\Delta\phi}{2}, p_{k+1} - \frac{\Delta\phi}{2} f_2), \tag{4.3}$$

$$f_4 = f(\phi_k, y_k), \tag{4.4}$$

$$p_k = p_{k+1} - \frac{\Delta\phi}{6}(f_1 + 2f_2 + 2f_3 + f_4), \tag{4.5}$$

where,

p_k, p_{k+1}: Discretized values of the vertical rolling pressure along the arc of contact;

f_i, $\forall i \in [1, ..., 4]$: Function values used in the numerical integration procedure;

ϕ_k, ϕ_{k+1}: Discretized arc values;

$\Delta\phi$: Angle interval for discretized arc.

In order to have an estimate of the roll gap temperature, the entrance and exit temperature of the roll gap are linearly interpolated to yield the estimated temperature. This estimated roll gap temperature along the arc of contact is used to calculate the yield stress of the material, the friction coefficient, and indirectly the position along the arc. The variation of speed along the arc of contact was not used in the calculation of the material yield stress, because the neutral point rolling mill speed and the associated geometric quantities are used to calculate an average strain and strain rate that the material is subjected to in the roll gap. This average strain and strain rate are used in the yield stress model see Eq. 3.28.

[5] As defined in table 3.1.

[6] $\frac{dp(\phi)}{d\phi} = 2R' \frac{p(\phi)}{h(\phi)} \left[\frac{sin\phi + \mu cos\phi}{1 - \mu tan\phi}\right] - 2R' \frac{(p(\phi) - k(\epsilon, \dot{\epsilon}, \theta))}{h(\phi)} sin\phi.$

[7] $\frac{dp(\phi)}{d\phi} = 2R' \frac{p(\phi)}{h(\phi)} \left[\frac{sin\phi - \mu cos\phi}{1 + \mu tan\phi}\right] - 2R' \frac{(p(\phi) - k(\epsilon, \dot{\epsilon}, \theta))}{h(\phi)} sin\phi.$

As was previously remarked in chapter 2, the neutral point shifts with the application of tension to the strip. A suitable equation was not found in the literature that defines the neutral point position as a function of the applied strip tensions. In order to evaluate the tension interactions with the roll gap model the modelling of the movement of the neutral point is fundamental in the calculation of the frictional forces in the roll gap.

The solution of the two differential equations are independent. At a certain point (neutral point) the solution of these two differential equations equate and the movement of the neutral point is thus solved numerically. In chapter 5 the effects of varying the applied strip tensions and the draft on the specific roll force are also highlighted using some illustrative figures.

4.3.2 Physical constants

In table 4.2 the roll radius as well as an average value for the roll radius and length of the arc of contact are shown. It was found that the logged data and the roll gap model simulation was not in agreement and the roll gap model was tuned to yield adequate roll force simulation. Two tuning parameters, α_{YS} and α_{RF}, were used. α_{YS} was used to tune the yield stress model to agree with calculated values in the database applicable to the Steckel Mill under investigation. After this step the roll force was tuned by adjusting, α_{RF}, and good agreement was achieved. In table 4.3 the yield stress model parameters and the tuning factors are shown.

Table 4.2: Roll gap model parameters

Variable	Value
R	375 mm
R'	403 mm
L_p	50 mm

Table 4.3: Yield stress model parameters and tuning factors. The yield stress model parameters are used in Eq. 3.28

Variable	Value
k_{fo}	2800
k_f	0.0024
k_{fspeed}	0.0165
α_{YS}	0.925
α_{RF}	0.716

4.3.3 Flow chart

In figure 4.4 the roll gap model flow chart is shown. The roll gap model has as its inputs the draft, main mill drive speed, exit and entrance temperatures, and the exit and entrance tensions that are outputs from the tension model. These variables are used to calculate the yield stress and friction coefficient along the arc of contact in order to find the vertical rolling force pressure along the arc of contact. It can be seen that the two independent differential equations are solved independently and when these solutions equate the neutral point is obtained. This array is combined and then integrated over the arc of contact to yield the rolling force. This rolling force is then used to calculate the deformed roll radius. This deformed roll radius is updated with an iterative Gauss-Seidel scheme and this loop terminates when the normalized error between two iterative steps is less than 0.1%. The Gauss-Seidel iterative scheme is described in more detail in section 4.4.2 where the tension model is discussed.

Once the neutral point is found, the velocity and thickness change along the arc of contact are calculated. The output of the roll gap model is the specific roll force, length of the arc of contact, and the entrance and exit velocities of the roll gap. These outputs are used as inputs for the other models in the mill simulator. The specific rolling force is used in the stand model. The length of the arc of contact is used in the main simulator loop to simulate the transport delay across the roll gap. The two speeds are used as inputs to the tension model.

4.4 Tension Model

4.4.1 Solution methodology

The implemented tension models are integrators with large gains. Classical control system theory [72] states that the bandwidth ($rad.s^{-1}$) is equal to the gain of the pure capacitive process. This gain is highly dependent on the constants of the system and is largely influenced by Young's modulus of the strip. In [73], Young's modulus for Stainless Steel grade 304, E_{ss}, is given as a function of temperature. Using the tabulated values in [73] an interpolated value of $E_{ss}|_{\theta=970°C} = 106 \times 10^9 Pa$ was found. The model gain is,

$$\frac{E_{ss}A_{cross}}{L_{cf\leftrightarrow rg}} = \frac{106 \times 10^9 wh_i}{6.4}, \forall i \in [1,2], \tag{4.6}$$

where A_{cross} is the cross sectional area of the strip in the width perpendicular to the rolling direction, and h_i is the thickness on either side of the roll gap. These gains determine the bandwidth, and also the simulation time interval of the model required to keep the tension model stable. The rule-of-thumb is to make the simulation frequency 2-10 times larger than the system bandwidth [74]. From Eq. 4.6, it is evident that the simulation frequency of the model lowers when the thickness decreases. This attests that tension control is of increasing importance with decreasing thickness as is the case for cold rolling mills and the latter passes of the rolling schedule for the Steckel Mill process. In order

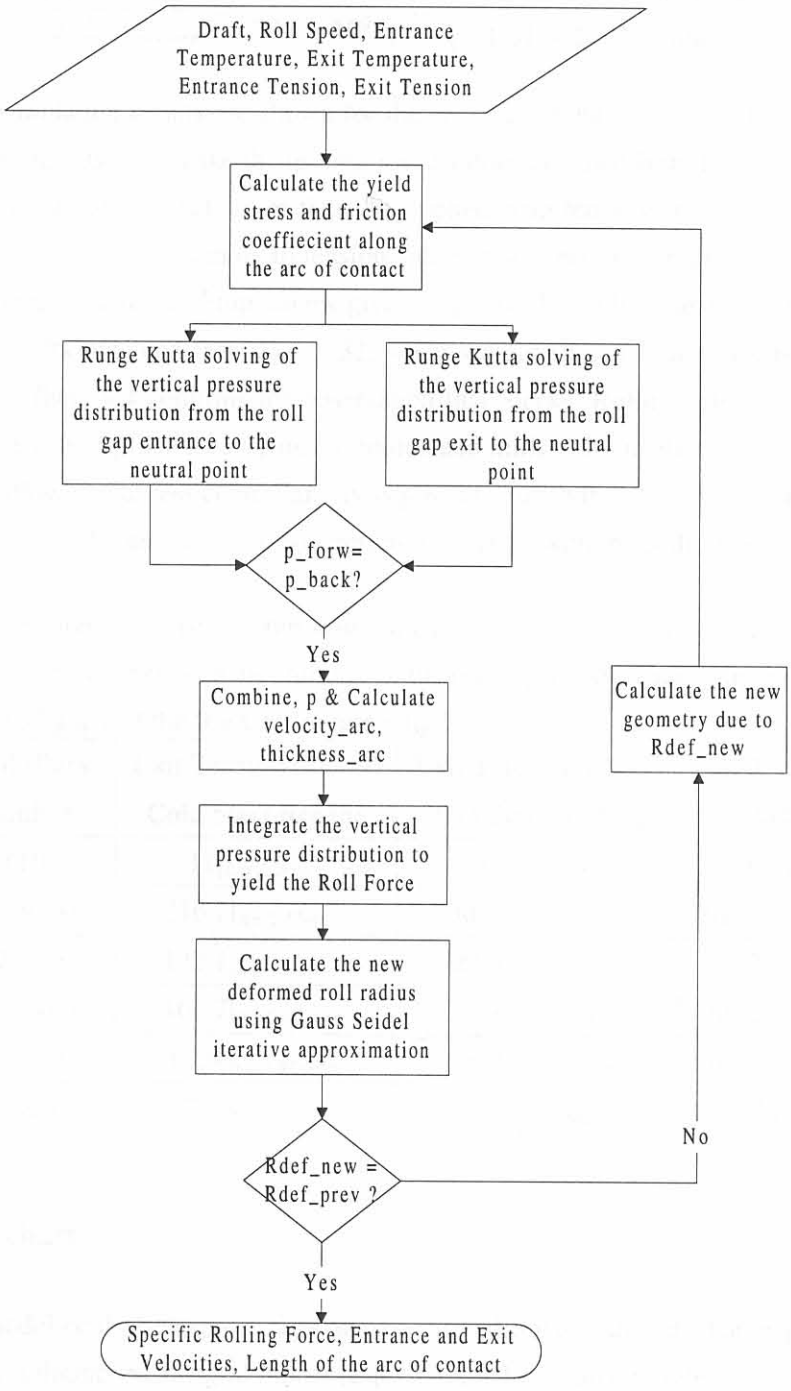

Figure 4.4: Roll gap model flowchart.

to save simulation time, the maximum allowable simulation time interval was chosen to correspond to a sampling frequency twice the bandwidth of the integrator model. The maximum simulation time intervals that can be used for the tension model simulation, when pass 3 data is used, are,

$$\Delta t_{tension} = \frac{2\pi}{2}\frac{L_{cf\leftrightarrow rg}}{E_{ss}A_{cross}} = \frac{1}{7.38\times 10^{9}h_i} = \begin{cases} 1.04\times 10^{-8}s, \; when\, h_i = 13mm \\ 1.51\times 10^{-8}s, \; when\, h_i = 9mm \end{cases} . \quad (4.7)$$

In chapter 5, simulation results are shown for the specific rolling force as a function of the applied tensions. These results may make the tension setup values obtained from Eq. 3.32 seem low. These setup tension values are in fact larger than the applied strip tensions associated with a multistand hot rolling mill, and are comparable to tension values associated with multistand cold rolling mills. In table 4.4, nominal tension setup values given in [3] for hot rolling and cold rolling of steel are compared to results obtained from Eq. 3.32, when similar strip thickness for both the hot rolling cases are used. Table 4.4 confirms the observation that Steckel Rolling relies on tension more as a secondary deformation process compared to multistand mills. Ultimately the strip can be drawn thin if necking[8] is allowed, but less controllability is possible due to the control effort associated with the acceleration and deceleration of the large inertias associated with the coiler motors and their drums.

Table 4.4: In this table the tension setup values are shown for various cases. The notation xB and xF refers to pass x's tension between the entrance of the roll gap and the back coiler and tension between the exit of the roll gap and the front coiler respectively.

Stand (Pass) Number	**Exit Tension (kN/m) Cold Steel Rolling**	**Exit Tension (kN/m) Hot Steel Rolling**	**Eq. 3.32 (kN/m) Steckel Rolling**
0 (1B)	$11\|_{h=2.2mm}$	$0\|_{h=22mm}$	$108.3\|_{h=22mm}$
1 (1F/2B)	$216.7\|_{h=1.65mm}$	$30.1\|_{h=11.57mm}$	$91.0\|_{h=11.57mm}$
2 (2F/3B)	$142.1\|_{h=0.96mm}$	$23.3\|_{h=6.30mm}$	$77.3\|_{h=6.30mm}$
3 (3F/4B)	$100.7\|_{h=0.61mm}$	$18.7\|_{h=3.97mm}$	$68.2\|_{h=3.97mm}$
4 (4F/5B)	$67.6\|_{h=0.41mm}$	$18.3\|_{h=2.95mm}$	$62.9\|_{h=2.95mm}$
5 (5F)	$17.1\|_{h=0.30mm}$	$5\|_{h=2.5mm}$	$60.2\|_{h=2.5mm}$

4.4.2 Flow chart

The tension model could be expressed as an explicit and implicit model. The explicit model is obtained by reformulating the integral model (Eqs. 3.33, 3.34) as an equivalent state-space differential equation model. The explicit model makes it difficult to solve for the implicit behaviour between the tensions applied to the roll gap model and the output velocities of the roll gap model. These velocities are in turn used as inputs to the tension model. Such an iterative process can be solved by using an iterative solution procedure such as Gauss-Seidel iteration.

[8] When the strip tension stress is larger that the material yield stress the strip deforms plastically. This deformation is manifested in a thickness and a less obvious width reduction of the sheet.

In this dissertation the tension model is kept unchanged in its integral format (Eqs. 3.33, 3.34). The input is the draft in the middle of the sheet, $\delta(z = 0, t = t_0)$, at any given time instance, which is an integer multiple of the main loop's simulation time interval, Δt_{Main}. In order to keep the tension loop stable it was found that, $\Delta t_{tension} < \Delta t_{Main}$, and that the tension loop must be solved at a higher frequency than the rest of the models.

It can be argued that due to these differences in the bandwidth of the tension processes and the rest of the simulator, that the tension models are faster than the rest of the processes, and could therefore be omitted from this study. Although there is some truth in this statement, this dissertation is an initial investigation into the tension and gauge interactions and no applicable article in the literature, where the effect of tension deviations on the thickness control loop of a Steckel Mill Process is investigated, could be found. However, statements are made in [3] that tension deviations influence the gauge control system of a single stand rolling mill adversely, and that Steckel Mills relies largely on a drawing process, which implies that the application of large tensions to the strip occurs.

In figure 4.5 two loops are apparent. The outer loop is the time loop that is simulated for time $t = t_0 + n\Delta t_{tension}, \forall t_0 \leq t \leq t_0 + \Delta t_{Main}$, where n is the simulation counter. The inner loop accounts for the iterative solution of the tension as a function of the exit and entrance speeds of the roll gap. The execution of this loop is stopped after the Gauss-Seidel filtered tension answer, $T_i; \forall i \in [1, 2]$,

$$T_i = \alpha T_{i_{new}} + (1 - \alpha) T_{i_{previous}}, \tag{4.8}$$

has stabilized to within a 0.1% error of the normalized tension differences between two iterative steps. This normalized error is expressed as,

$$error_T = \frac{|T_1 - T_{1_{previous}}|}{T_{1_{previous}}} + \frac{|T_2 - T_{2_{previous}}|}{T_{2_{previous}}}, \tag{4.9}$$

where $T_{i_{new}}$ is the current calculated tension due to speed deviations obtained from the roll gap model after $T_{i_{previous}}$ was applied to the roll gap model. This new tension value is filtered in order to ensure convergence and to negate possible divergent oscillating. Before the execution of the next iterative step, $T_{i_{previous}}$ is set equal to the current T_i.

The tension loop executes rapidly if $\alpha = 0.95$. A safety factor of 15 loop iterations is set as the maximum number of iterative steps. After the completion of the loop the tension value is used in the rest of the simulator at the timing instance of the main loop.

4.5 Stand Model

4.5.1 Solution Methodology

Separation of variables

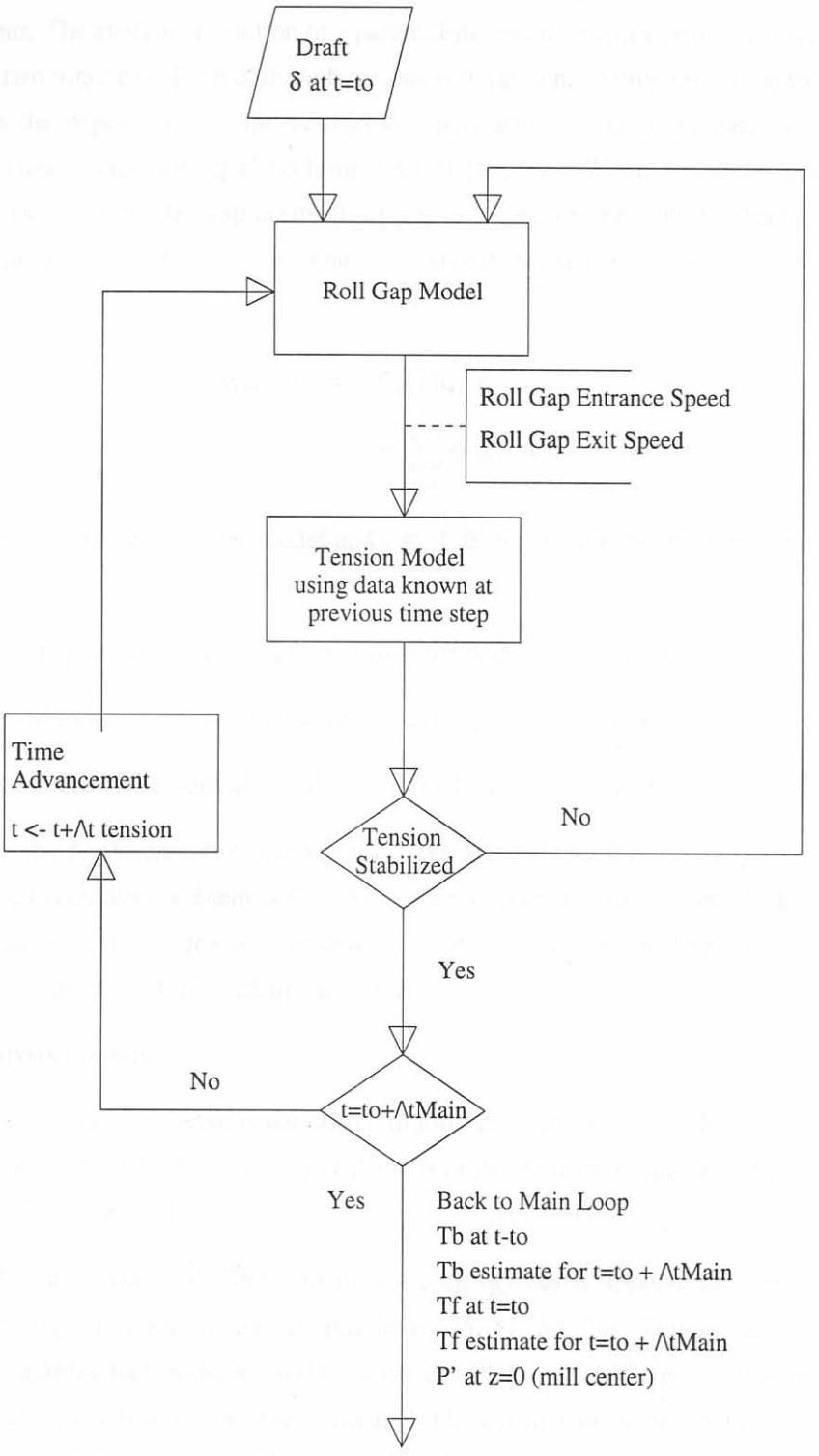

Figure 4.5: Flow Diagram used in the solution of the tension model

There are different ways of solving a partial differential equation model [75, 51, 53, 54, 7] such as depicted in chapter 3. It was decided to use an analytical approximate method [75] to solve the vertical displacements of the rollers as a function of time and space in order to simulate the strip crown behaviour. The analytical solution of a partial differential equation requires that the variable be separated into two functions. Each of these functions is dependent on only one of the two independent variables, thus the dependence of the vertical displacements $y(z,t)$ is separated into two infinite vectors, $\Phi(z)$ (row vector) and $\mathbf{q}(t)$ (column vector) [53, 54]. When the vector product is taken between these two vectors, the displacement, $y(z,t)$ is a superposition of an infinite number of the products $\phi_j(z)q_j(t)$ $(\forall j \in [0,1,2,...])$. Thus the vertical displacements of the stand model can be expressed as:

$$\begin{aligned} y_i(z,t) &= \Phi_i(z)\mathbf{q}_i(t) \\ &= \sum_{j=0}^{\infty} \phi_{i_j}(z)q_{i_j}(t), \end{aligned} \tag{4.10}$$

where $i \in [1,2,3,4]$ for the 4 roller model and $i \in [1,2]$ for the 2 roller pack model. The variables are,

$y_i(z,t)$: Vertical displacement in time of a roll over the width of the rolling mill stand.

$\Phi_i(z)$: The natural mode of vibration (row vector) for a continuous system.

$\mathbf{q}_i(t)$: Column vectors of the normal coordinates, which are continuous functions of time.

The solution for the displacements of the beams can be obtained by solving the Eigenvalue problem of the system. The Eigenvalue problem is solved to generate ordinary and independent sets of ordinary differential equations that will describe the dynamic motion of the system. The calculated eigenvalues are the natural frequencies of the undamped system.

Vibration analysis method

The more common ways to derive equations of motion are with the aid of Newtonian dynamics or Lagrange dynamics [54, 53]. Although more degrees of freedom are required to describe a system if Newtonian dynamics are used.

The Raleigh-Ritz and Assumed Modes method are energy-based approximate analytical methods used for the solving of vibration analysis problems [75, 52, 53, 76]. It was stated earlier that the separation of variables technique is used to solve the PDE model. It is not feasible to calculate the infinite modes of vibration, but the vertical displacement can be approximated by taking the superposition of the products of a finite number of modes of vibration and their accompanying normal coordinates.

The approximate vertical displacement is expressed as,

$$y_i(z,t) \approx \sum_{j=0}^{2p} \phi_{i_j}(z) q_{i_j}(t), \ \forall i \in [1,2,3,4], \tag{4.11}$$

where p is the number of accurate natural modes of vibration.

For the Assumed Modes and the Rayleigh Ritz method the number of modes ($2p$) is chosen two times larger than the predominant spatial modes (p) [75].

Each roller has $2p$ number of assumed modes. Application of the Assumed Modes method only requires that the assumed modes be generated for one element. The same modes can be used for the other roller elements. The assumed modes must satisfy the boundary values given in equations 3.64, 3.65, 3.66, 3.67, 3.69, 3.70, 3.71 and 3.72. From these equations it can be seen that each of the roller elements have the same boundary value structure[9]. In this work the choice of the assumed modes is motivated by the results obtained by Pederson [59], where the first two natural modes of vibration were calculated using Galerkin's method[10]. In this dissertation four assumed modes were developed although not all of these modes are used in the implemented simulator. When the number of assumed modes increase with one, the number of states of the stand model increases with 2 for each roller. The generated assumed modes[11] for one roller are shown in figure 4.6 and are given as,

$$\Psi_i = \begin{bmatrix} \psi_{i_1} & \psi_{i_2} & \psi_{i_3} & \psi_{i_4} \end{bmatrix}, \ \forall i \in [1,2,3,4], \tag{4.12}$$

where the first assumed modes is,

$$\psi_{i_1}(z) = 4.25\left(\frac{2z}{l_i}\right)^3 - 1.28\left(\frac{2z}{l_i}\right) - 0.5, \tag{4.13}$$

the second assumed mode,

$$\psi_{i_2}(z) = 0.15\left(\frac{2z}{l_i}\right)^4 - 0.3\left(\frac{2z}{l_i}\right)^2 + 1.0, \tag{4.14}$$

the third assumed mode,

$$\psi_{i_3}(z) = -2.81\left(\frac{2z}{l_i}\right)^5 - 5.38\left(\frac{2z}{l_i}\right)^3 + 2.06\left(\frac{2z}{l_i}\right) - 0.5, \tag{4.15}$$

and the fourth assumed mode is,

$$\psi_{i_4}(z) = 7.11\left(\frac{2z}{l_i}\right)^6 - 14.22\left(\frac{2z}{l_i}\right)^4 + 7.11\left(\frac{2z}{l_i}\right)^2. \tag{4.16}$$

[9] $y_i^{(1)}\Big|_{z=\frac{\pm l_i}{2}} = 0$ and $y_i^{(3)}\Big|_{z=\frac{\pm l_i}{2}} \neq 0$, $\forall i \in [1,2,3,4]$, where $^{(n)}$ signifies a nth order differentiation of space (z).

[10] Galerkin's method is another approximate analytical method used for solving PDE models [75].

[11] The normal structure of the natural modes of vibration for a simple beam is [59, 60, 53], $\phi_i(z) = c_{i1}cos\beta_i z + c_{i2}sin\beta_i z + c_{i3}cosh\beta_i z + c_{i4}sinh\beta_i z$.

The coupled assumed modes of vibration for the four roller model are, $\mathbf{\Psi} = \begin{bmatrix} \Psi_1 & \Psi_2 & \Psi_3 & \Psi_4 \end{bmatrix}$, and for the two roll pack, $\mathbf{\Psi} = \begin{bmatrix} \Psi_1 & \Psi_2 \end{bmatrix}$, where $\mathbf{\Psi}$ is a row vector.

Taking the assumed modes of the approximate method into consideration, an estimate of the vertical displacement, $\widehat{y_i}$, can be expressed as,

$$\widehat{y_i}(z,t) = \sum_{j=1}^{2p} \psi_{i_j}(z) q_{i_j}(t) = \Psi_i(z)\mathbf{q}_i(t), \ \forall i \in [1,2,3,4]. \tag{4.17}$$

The spatial solution, $\mathbf{\Phi}(z)$, of the stand model is obtained by solving the Eigenvalue problem of the system. When the Eigenvalue problem is solved, the system can be decoupled, and a set of ordinary differential equations for the normal time coordinates $\mathbf{q}(t)$, is obtained. The relationship between the assumed modes and the natural modes of vibrations is [54, 75],

$$\mathbf{\Phi}(z) = \mathbf{\Psi}(z)\mathbf{U}, \tag{4.18}$$

where $\mathbf{U}$ is the modal matrix of the system [54].

For the purposes of the simulator it was decided to concentrate on the two roll pack model, because the four roller model increases the complexity of the mill simulator and increases the simulation time. Other reasons for this choice are given in section 3.5.6.

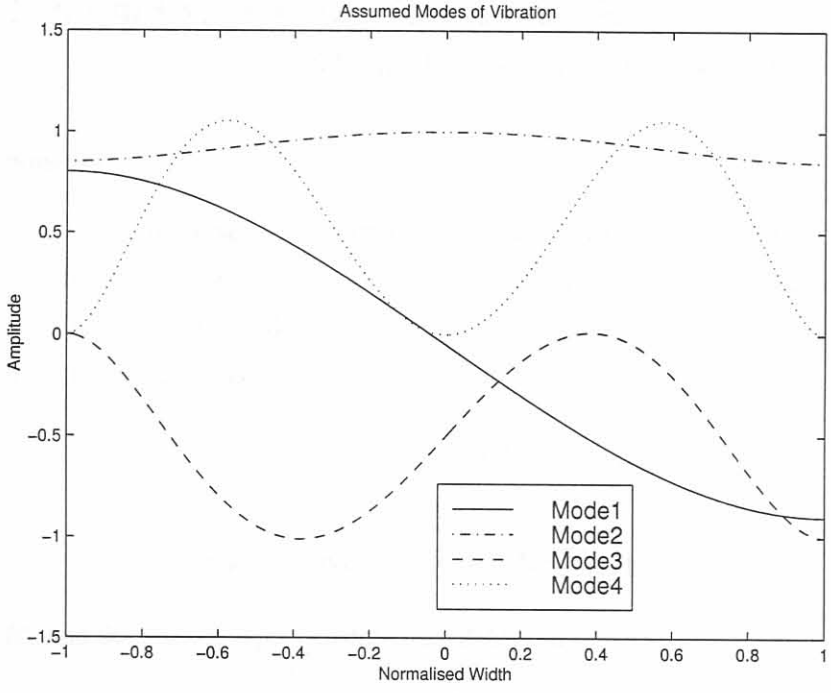

Figure 4.6: Assumed Modes for a roller element

4.5.2 Two Roller model

4.5.2.1 Model equations

Roll Packs

In order to avoid confusion with the indices in this section and the indices used in chapter 3, the indices of the two roll packs, namely $_{12}$ and $_{34}$ are renamed as $_1$ and $_2$ respectively.

When Eq. 4.17 is substituted into Eqs. 3.63 and 3.68, while a fourth order spatial derivative as well as a second and first derivative of time are done, for the estimated vertical displacement of each roller[12],

$$\rho A_1 \Psi_1 \ddot{\mathbf{q}}_1 + EI_1 \Psi_1^{(4)} \mathbf{q}_1 + \beta_{strip} \Psi_1 \dot{\mathbf{q}}_1 + k_{strip} \Psi_1 \mathbf{q}_1 = +k_{strip} \Psi_2 \mathbf{q}_2 + \beta_{strip} \Psi_2 \dot{\mathbf{q}}_2 + P', \quad (4.19)$$

$$\rho A_2 \Psi_2 \ddot{\mathbf{q}}_2 + EI_2 \Psi_2^{(4)} \mathbf{q}_2 + \beta_{strip} \Psi_2 \dot{\mathbf{q}}_2 + k_{strip} \Psi_2 \mathbf{q}_2 = +\beta_{strip} \Psi_1 \dot{\mathbf{q}}_1 + k_{strip} \Psi_1 \mathbf{q}_1 - P'. \quad (4.20)$$

Premultiplying Eq. 4.19 and Eq. 4.20 with $\Psi_1^T(z)$ and $\Psi_2^T(z)$ respectively yields,

$$\begin{aligned} \Psi_1^T \rho A_1 \Psi_1 \ddot{\mathbf{q}}_1 + \Psi_1^T EI_1 \Psi_1^{(4)} \mathbf{q}_1 + \Psi_1^T \beta_{strip} \Psi_1 \dot{\mathbf{q}}_1 + \Psi_1^T k_{strip} \Psi_1 \mathbf{q}_1 = \\ +\Psi_1^T \beta_{strip} \Psi_2 \dot{\mathbf{q}}_2 + \Psi_1^T k_{strip} \Psi_2 \mathbf{q}_2 + \Psi_1^T P', \end{aligned} \quad (4.21)$$

$$\begin{aligned} \Psi_2^T \rho A_2 \Psi_2 \ddot{\mathbf{q}}_2 + \Psi_2^T EI_2 \Psi_2^{(4)} \mathbf{q}_2 + \Psi_2^T \beta_{strip} \Psi_2 \dot{\mathbf{q}}_2 + \Psi_2^T k_{strip} \Psi_2 \mathbf{q}_2 = \\ +\Psi_2^T \beta_{strip} \Psi_1 \dot{\mathbf{q}}_1 + \Psi_2^T k_{strip} \Psi_1 \mathbf{q}_1 - \Psi_2^T P'. \end{aligned} \quad (4.22)$$

Discrete Components

The interactions between the discrete elements associated with the hydraulic jacks, the work roll chock-bearing combinations as well as the forces (these forces work in tandem and are taken as the same force, $J(t)$) that can be exerted by the hydraulic jacks in order to apply positive or negative work roll bending, are expressed as,

$$M_{sJT} \ddot{y}_{sJT} + K_{sJ} y_{sJT} = J(t) + K_{sJ} y_{sJB}, \quad (4.23)$$

$$M_{sJB} \ddot{y}_{sJB} + K_{sJ} y_{sJB} = -J(t) + K_{sJ} y_{sJT}, \quad (4.24)$$

where $s \in [L, R]$, and the generic representations are defined as:

M_{sJT}, M_{sJB}: The masses of the top and bottom work roll chock-bearing combinations.

K_{sJ}: The hydraulic stiffness of the hydraulic actuators and unmodelled stiffness lumped together to form a discrete spring on either side of the mill.

[12]The notation applies $\gamma^{(n)}(\tau) = \frac{\partial^n \gamma}{\partial \tau^n}$, thus $^{(n)}$ denotes an $n^{(th)}$ order spatial derivative of the displacement variable.

y_{sJT}, y_{sJB}: The vertical displacements of the lumped discrete elements M_{sJT}, M_{sJB} (also see figure 3.3).

The interactions between the discrete elements associated with the back-up chock-bearing combinations and the hydraulic actuators and load cells are expressed as,

$$M_{sT}\ddot{y}_{sT} = -F_{HAs}, \tag{4.25}$$

$$M_{sB}\ddot{y}_{sB} + K_{sB}y_{sB} = 0, \tag{4.26}$$

where $s \in [L, R]$, and the generic representations are defined as:

M_{sT}, M_{sB}: The masses of the top and bottom back-up roll chock-bearing combinations.

K_{sB}: The stiffness of the load cells on either side of the mill.

F_{HAs}: The thrust force of the hydraulic actuators.

y_{sB}, y_{sT}: The vertical displacements of the lumped discrete elements M_{sT}, M_{sB} (also see figure 3.3).

The displacements at the end of the rollers and the displacement of the discrete elements are the same displacement and provide the connecting relationship between the discrete and the continuous systems. These displacements are expressed as,

$$y_{LT}(t) = y_{LJT}(t) = y_1(\frac{-l_1}{2}, t) \approx \Psi_1(\frac{-l_1}{2})\mathbf{q}_1(t), \tag{4.27}$$

$$y_{RT}(t) = y_{RJT}(t) = y_1(\frac{l_1}{2}, t) \approx \Psi_1(\frac{l_1}{2})\mathbf{q}_1(t), \tag{4.28}$$

$$y_{LB}(t) = y_{LJB}(t) = y_2(\frac{-l_2}{2}, t) \approx \Psi_2(\frac{-l_2}{2})\mathbf{q}_2(t), \tag{4.29}$$

$$y_{RB}(t) = y_{RJB}(t) = y_2(\frac{l_2}{2}, t) \approx \Psi_2(\frac{l_2}{2})\mathbf{q}_2(t). \tag{4.30}$$

When the above relationships are substituted into equations 4.23, 4.24, 4.25 and 4.26. The resulting eight equations of motion are premultiplied with $\Psi_1^T(\frac{-l_1}{2})$, $\Psi_1^T(\frac{l_1}{2})$, $\Psi_2^T(\frac{-l_2}{2})$ and $\Psi_2^T(\frac{l_2}{2})$ consecutively. The following equations result,

$$\Psi_1^T(\frac{-l_1}{2})M_{LT}\Psi_1(\frac{-l_1}{2})\ddot{\mathbf{q}}_1 = \Psi_1^T(\frac{-l_1}{2})F_{HAL}, \tag{4.31}$$

$$\Psi_1^T(\frac{l_1}{2})M_{RT}\Psi_1(\frac{l_1}{2})\ddot{\mathbf{q}}_1 = \Psi_1^T(\frac{l_1}{2})F_{HAR}, \tag{4.32}$$

$$\Psi_2^T(\frac{-l_2}{2})M_{LB}\Psi_2(\frac{-l_2}{2})\ddot{\mathbf{q}}_2 + \Psi_2^T(\frac{-l_2}{2})K_{LB}\Psi_2(\frac{-l_2}{2})\mathbf{q}_2 = 0, \tag{4.33}$$

$$\Psi_2^T(\frac{l_2}{2})M_{RB}\Psi_2(\frac{l_2}{2})\ddot{\mathbf{q}}_2 + \Psi_2^T(\frac{l_2}{2})K_{RB}\Psi_2(\frac{l_2}{2})\mathbf{q}_2 = 0, \tag{4.34}$$

$$\Psi_1^T(\frac{-l_1}{2})M_{LJT}\Psi_1(\frac{-l_1}{2})\ddot{\mathbf{q}}_1 + \Psi_1^T(\frac{-l_1}{2})K_{JL}\Psi_1(\frac{-l_1}{2})\mathbf{q}_1 = \Psi_1^T(\frac{-l_1}{2})K_{JL}\Psi_2(\frac{-l_1}{2})\mathbf{q}_2 + \Psi_1^T(\frac{-l_1}{2})J, \tag{4.35}$$

$$\Psi_1^T(\frac{l_1}{2})M_{RJT}\Psi_1(\frac{l_1}{2})\ddot{\mathbf{q}}_1 + \Psi_1^T(\frac{l_1}{2})K_{JR}\Psi_1(\frac{l_1}{2})\mathbf{q}_1 = \Psi_1^T(\frac{l_1}{2})K_{JR}\Psi_2(\frac{l_2}{2})\mathbf{q}_2 + \Psi_1^T(\frac{l_1}{2})J, \tag{4.36}$$

$$\Psi_2^T(\frac{-l_2}{2})M_{LJB}\Psi_2(\frac{-l_2}{2})\ddot{\mathbf{q}}_2 + \Psi_2^T(\frac{-l_2}{2})K_{JL}\Psi_2(\frac{-l_2}{2})\mathbf{q}_2 = \Psi_2^T(\frac{-l_2}{2})K_{JL}\Psi_1(\frac{-l_1}{2})\mathbf{q}_1 - \Psi_2^T(\frac{-l_2}{2})J, \tag{4.37}$$

$$\Psi_2^T(\frac{l_2}{2})M_{RJT}\Psi_2(\frac{l_2}{2})\ddot{\mathbf{q}}_2 + \Psi_2^T(\frac{l_2}{2})K_{JR}\Psi_2(\frac{l_2}{2})\mathbf{q}_2 = \Psi_2^T(\frac{l_2}{2})K_{JR}\Psi_1(\frac{l_1}{2})\mathbf{q}_1 - \Psi_2^T(\frac{l_2}{2})J. \tag{4.38}$$

The total stand model in terms of the assumed modes is obtained when equations associated with the top roll pack and equations associated with the bottom roll pack are summed respectively. In the following sections the whole stand model is manipulated to yield a linear state-space matrix model.

4.5.2.2 Mass, stiffness and damping elements

In order to express the stand model in linear matrix notation, the mass, stiffness and damping matrices of each element have to be computed.

Continuous Masses

The mass matrix of each continuous mass roller are expressed as $\mathbf{M}_{ij} \in \Re^{2p\times 2p}, \forall i,j \in [1,2]$. The matrix elements of the estimated mass matrices associated with the rollers are obtained, when the following integrals are done over the width of the rollers:

$$m_{i_h j_g} = \begin{cases} \int_{\frac{-l_i}{2}}^{\frac{l_i}{2}} \psi_{i_h}\rho A_i \psi_{j_g} dz, \ \forall i = j \ and \ i \in [1,2] \\ 0, \ \forall i \neq j \end{cases}, \tag{4.39}$$

where $h, g \in [1, ..., 2p]$.

Discrete bearing mass elements

The matrices for the discrete mass elements are constructed as follows,

$$\mathbf{M}_{dsi} = \Psi_i(z)^T M_{s\chi}\Psi_i(z), \in \Re^{2p\times 2p}, \tag{4.40}$$

$$\mathbf{M}_{dJsi} = \Psi_i(z)^T M_{Js\chi}\Psi_i(z), \in \Re^{2p\times 2p}, \tag{4.41}$$

where s, i, j, χ are indices and $s \in [L, R]$. When $s = L \Rightarrow z = -\frac{l_i}{2}$, $s = R \Rightarrow z = \frac{l_i}{2}$. When $i = 1 \Rightarrow \chi = T$, and when $i = 2 \Rightarrow \chi = B$.

Bending Stiffness of Roller Elements

After the substitution of the assumed vertical displacement into the PDE-model as shown in equations 4.21 and 4.22, the bending stiffness of a roller pack needs to be calculated as,

$$k_{i_g i_h} = \int_0^{l_i} \psi_{i_g} EI_i \psi_{i_h}^{(4)} dz. \tag{4.42}$$

But in [75] it is shown that the assumed bending stiffness of a beam is calculated as,

$$k_{i_g i_h} = \int_0^{l_i} \psi_{i_g}^{(2)} EI_i \psi_{i_h}^{(2)} dz, \tag{4.43}$$

where the latter equation is obtained by following a Lagrangian dynamic approach. The discrepancy between the order of spatial differentiation of the assumed modes between Eq. 4.43 and Eq. 4.42, can be clarified by observing from [54] that the natural bending stiffness of a beam is calculated as,

$$k_{i_g i_h} = \int_0^{l_i} \phi_{i_g}^{(2)} EI_i \phi_{i_h}^{(2)} dz, \tag{4.44}$$

but if the true vertical displacement, $y = \Phi \mathbf{q}$, is substituted into the PDE model (Eqs. 3.63 and 3.68) the bending stiffness would be calculated as,

$$k_{i_g i_h} = \int_0^{l_i} \phi_{i_g} EI_i \phi_{i_h}^{(4)} dz, \tag{4.45}$$

When integration by parts is done twice on Eq. 4.45 the following is yielded,

$$\int_{\frac{-l}{2}}^{\frac{l}{2}} \phi(x)\phi^{(4)}(x)dx = \phi(x)\phi^{(3)}(x)|_{\frac{-l}{2}}^{\frac{l}{2}} - \phi^{(1)}(x)\phi^{(2)}(x)|_{\frac{-l}{2}}^{\frac{l}{2}} + \int_{\frac{-l}{2}}^{\frac{l}{2}} \phi^{(2)}(x)\phi^{(2)}(x)dx, \tag{4.46}$$

and it can be shown that $\int_{\frac{-l}{2}}^{\frac{l}{2}} \phi(z)\phi^{(4)}(z)dz = \int_{\frac{-l}{2}}^{\frac{l}{2}} \phi^{(2)}(z)\phi^{(2)}(z)dz$, but $\int_{\frac{-l}{2}}^{\frac{l}{2}} \psi(z)\psi^{(4)}(z)dz$ is not necessarily equal to $\int_{\frac{-l}{2}}^{\frac{l}{2}} \psi^{(2)}(z)\psi^{(2)}(z)dz$. The relationship (see Eq. 4.18) between the assumed modes and the natural modes of vibration ensures that the real bending stiffness will be computed after the solution of the Eigenvalue problem. Thus Eq. 4.43 is used in the calculation of the assumed bending stiffness of a roll pack. Thus,

$$k_{i_h i_g} = \begin{cases} \int_0^{l_i} \psi_{i_k}^{(2)}(z) EI_i(z) \psi_{j_g}^{(2)}(z)dz, \ \forall i = j \ and \ i \in [1,2] \\ 0, \ \forall i \neq j \end{cases}, \tag{4.47}$$

where $h, g \in [1, 2]$.

Elastic Recovery of Strip

From Eqs. 4.21 and 4.22 it is seen that the elastic recovery of the strip is modelled as a distributed spring element. The matrix elements can be calculated as,

$$k_{strip_{i_h j_g}} = \int_{-\frac{w}{2}}^{\frac{w}{2}} \psi_{i_h}(z) k_{strip}(z) \psi_{j_g}(z)dz, \tag{4.48}$$

where $k_{strip_{i_h j_g}} \in \mathbf{K}_{strip_{ij}}$, and the elastic recovery stiffness matrix is expressed as,

$$\mathbf{K}_{strip} = \begin{bmatrix} \mathbf{K}_{strip_{11}} & -\mathbf{K}_{strip_{12}} \\ -\mathbf{K}_{strip_{21}} & \mathbf{K}_{strip_{22}} \end{bmatrix} \in \Re^{2p \times 2p} \tag{4.49}$$

Load Cell Discrete Spring Elements

From Eqs. 4.33 and 4.34 the discrete stiffness matrix associated with the load cells is calculated as,

$$\mathbf{K}_{ds2} = \Psi_2(z)^T K_{sB} \Psi_2(z) \in \Re^{2p \times 2p}, \tag{4.50}$$

where $s \in [L, R]$ and $\mathbf{K}_{ds2} \in \Re^{2p \times 2p}$. When $s = L \Rightarrow z = -\frac{l_i}{2}$, $s = R \Rightarrow z = \frac{l_i}{2}$.

Hydraulic Jacks Springs elements

From Eqs. 4.35-4.38 the discrete stiffness matrix associated with the hydraulic jack springs is calculated as,

$$\mathbf{K}_{Jdijs} = \Psi_i(z)^T K_{Js} \Psi_j(z), \tag{4.51}$$

where $s \in [L, R]$ and $\mathbf{K}_{Jdijs} \in \Re^{2p \times 2p}$. When $s = L \Rightarrow z = -\frac{l_i}{2}$, $s = R \Rightarrow z = \frac{l_i}{2}$. When $i = 1 \Rightarrow \chi = T$, and when $i = 2 \Rightarrow \chi = B$.

Strip/Work Roll Damping

From Eqs. 4.21 and 4.22 it is seen that the damping is also modelled as a distributed parameter. The damping matrix elements are calculated as,

$$C_{i_h j_g} = \int_{-\frac{w}{2}}^{\frac{w}{2}} \psi_{i_h}(z) \beta_{strip}(z) \psi_{j_g}(z) dz, \tag{4.52}$$

where $C_{i_h j_g} \in \mathbf{C}_{ij} \in \Re^{2p \times 2p}$.

Total Stand Model

When the above matrices are summed the assumed modes mass and stiffness matrices are obtained as,

$$\widehat{\mathbf{M}} = \begin{bmatrix} \mathbf{M}_{11} + \mathbf{M}_{dL1} + \mathbf{M}_{dR1} & \mathbf{0} \\ +\mathbf{M}_{dJL1} + \mathbf{M}_{dJR1} & \\ \mathbf{0} & \mathbf{M}_{22} + \mathbf{M}_{dL2} + \mathbf{M}_{dR2} \\ & +\mathbf{M}_{dJL2} + \mathbf{M}_{dJR2} \end{bmatrix} \in \Re^{4p \times 4p}, \tag{4.53}$$

$$\widehat{\mathbf{K}} = \begin{bmatrix} \mathbf{K}_{11} + \mathbf{K}_{strip_{11}} + \mathbf{K}_{Jd11L} & -\mathbf{K}_{strip_{12}} - \mathbf{K}_{Jd12L} - \mathbf{K}_{Jd12R} \\ +\mathbf{K}_{Jd11R} & \\ -\mathbf{K}_{strip_{21}} - \mathbf{K}_{Jd21L} - \mathbf{K}_{Jd21R} & \mathbf{K}_{22} + \mathbf{K}_{strip_{22}} + \mathbf{K}_{Jd22L} \\ & +\mathbf{K}_{Jd22R} + \mathbf{K}_{dL2} + \mathbf{K}_{dR2} \end{bmatrix} \in \Re^{4p \times 4p}. \tag{4.54}$$

The assumed damping matrix of the stand model is expressed as,

$$\widehat{\mathbf{C}} = \begin{bmatrix} \mathbf{C}_{11} & -\mathbf{C}_{12} \\ -\mathbf{C}_{21} & \mathbf{C}_{22} \end{bmatrix} \in \Re^{4p \times 4p}. \tag{4.55}$$

Taking Eq. 4.18 into account the coupled stand model equations of motion can be expressed as,

$$\widehat{\mathbf{M}}\mathbf{U}\ddot{\mathbf{q}} \ + \widehat{\mathbf{C}}\mathbf{U}\dot{\mathbf{q}} + \ \widehat{\mathbf{K}}\mathbf{U}\mathbf{q} = \mathbf{B}\mathbf{u} \tag{4.56}$$

4.5.2.3 Discretization

The continuous mass rollers were discretized into 50 discrete elements with 51 nodes. The distance between two nodes is expressed as Δ_z, which is equal to 8cm. Using these discrete nodes the integrals can be solved using Boole's numerical integration method [71] or normal Euler numerical integration. The areas and second moments of inertias were diagonalized[13] and the assumed modes were evaluated at each node[14].

Different values of p was experimented with but in the final simulator p was taken as one. In [59] a total of 2 vibration modes were used and in [40] three modes of vibration are used as the rollers are large and stiff elements, which limit high order spatial bending modes.

4.5.2.4 Solution

The modal matrix is solved from the general Eigenvalue problem,

$$(\widehat{\mathbf{K}} - \omega^2\widehat{\mathbf{M}})\mathbf{U} = 0, \tag{4.57}$$

where $\mathbf{U} \in \Re^{4p \times 4p}$.

The decoupled equation of motion of the stand is written as,

$$\mathbf{U}^{\mathrm{T}}\widehat{\mathbf{M}}\mathbf{U}\ddot{\mathbf{q}} \ + \mathbf{U}^{\mathrm{T}}\widehat{\mathbf{C}}\mathbf{U}\dot{\mathbf{q}} + \ \mathbf{U}^{\mathrm{T}}\widehat{\mathbf{K}}\mathbf{U}\mathbf{q} = \mathbf{U}^{\mathrm{T}}\mathbf{B}\mathbf{u} \tag{4.58}$$

where $\mathbf{M} = \mathbf{U}^{\mathrm{T}}\widehat{\mathbf{M}}\mathbf{U}$, $\mathbf{K} = \mathbf{U}^{\mathrm{T}}\widehat{\mathbf{K}}\mathbf{U}$, $\mathbf{C} = \mathbf{U}^{\mathrm{T}}\widehat{\mathbf{C}}\mathbf{U}$ and $\mathbf{q} = \begin{bmatrix} q_{1_1} & q_{1_2} & q_{2_1} & q_{2_2} \end{bmatrix}^T \in \Re^{2(2p)\times 1}$[15].

The decoupled normal coordinate system is expressed as,

$$\begin{bmatrix} \dot{\mathbf{q}} \\ \ddot{\mathbf{q}} \end{bmatrix} = \begin{bmatrix} \mathbf{I}_{2p\times 2p} & 0 \\ -\mathbf{M}^{-1}\mathbf{K} & -\mathbf{M}^{-1}\mathbf{C} \end{bmatrix} \begin{bmatrix} \mathbf{q} \\ \dot{\mathbf{q}} \end{bmatrix} + \begin{bmatrix} 0 \\ \mathbf{M}^{-1}\mathbf{U}^{\mathrm{T}}\mathbf{B} \end{bmatrix} \mathbf{u} \tag{4.59}$$

where $\mathbf{B}$ and $\mathbf{u}$ are the input matrix and input vector respectively. In section 4.7 these variables are defined.

[13] $A_i(z) = diag\{A\} \in \Re^{51\times 51}$, $I_i(z) = diag\{I\} \in \Re^{51\times 51}$, where $i \in [1, 2]$.

[14] $\Psi_i \in \Re^{51\times 2p}$

[15] The notation $q_{\#roll_{\#assumed\ mode}}$ applies.

The natural modes of vibration of the stand model are calculated by using the calculated modal matrix and the assumed modes vector as shown in Eq. 4.18. In figures 4.7, 4.8, 4.9 and 4.10 the natural modes of vibration for the two roller pack case, where the number of assumed modes is 3 and 4, are shown. In figures 4.11 and 4.12 the natural modes of vibration for two different cases when the number of assumed modes is 2 are shown. The distinguishing factor between these two cases is whether the hydraulic jacks were modelled or not, e.g. $K_{sJ} = 0$ (figure 4.11) or $K_{sJ} = 8e10\frac{N}{m}$ (figure 4.12).

The discretized vertical displacements are calculated as,

$$\mathbf{y} = \begin{bmatrix} y_{1_{\Delta_z}} \\ y_{2_{\Delta_z}} \end{bmatrix} = \begin{bmatrix} \Phi_1 & \Phi_2 \end{bmatrix} \begin{bmatrix} \mathbf{q}_1 \\ \mathbf{q}_2 \end{bmatrix}, \tag{4.60}$$

where $y_{1_{\Delta_z}}, y_{2_{\Delta_z}} \in \Re^{51\times 1}$.

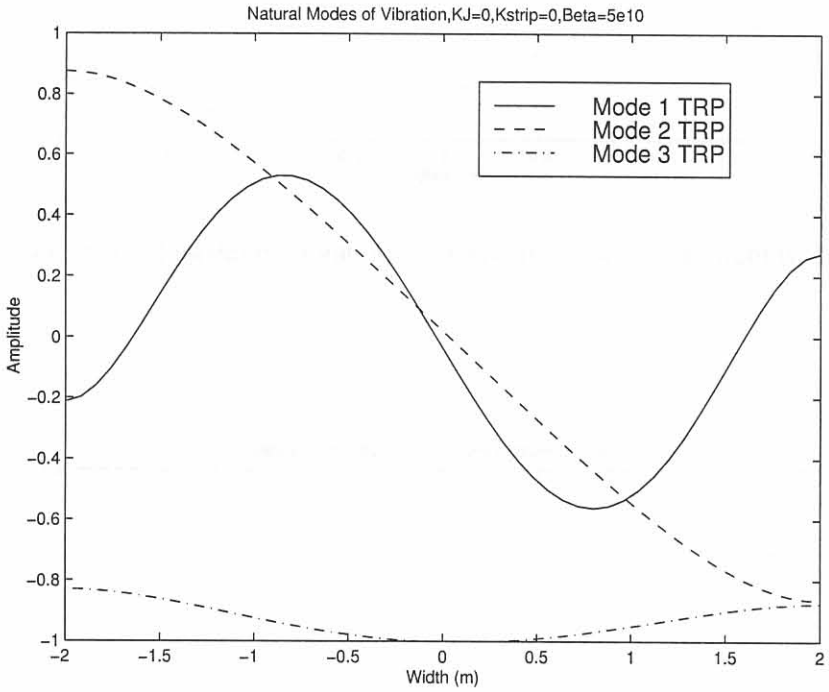

Figure 4.7: Natural modes of vibration for 3 assumed modes of Top Roll Pack.

4.5.2.5 Flowchart

The solution of the stand model only requires matrix operations and a Runge Kutta time integration. The Runge Kutta procedure is used on the total simulator nonlinear state-space model. This will be discussed in section 4.7.

4.5.3 Physical constants

Roller Weights

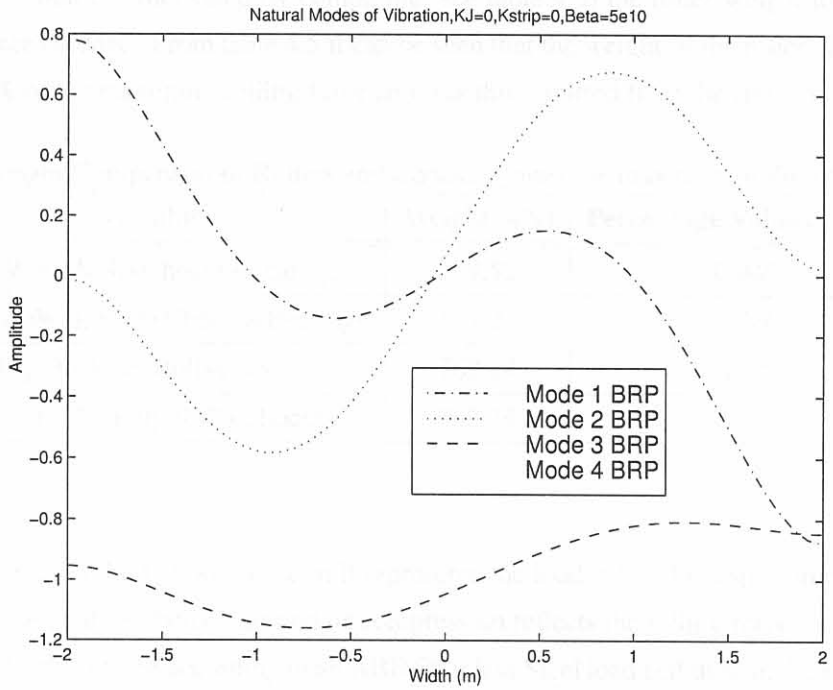

Figure 4.8: Natural modes of vibration for 3 assumed modes of Bottom Roll Pack.

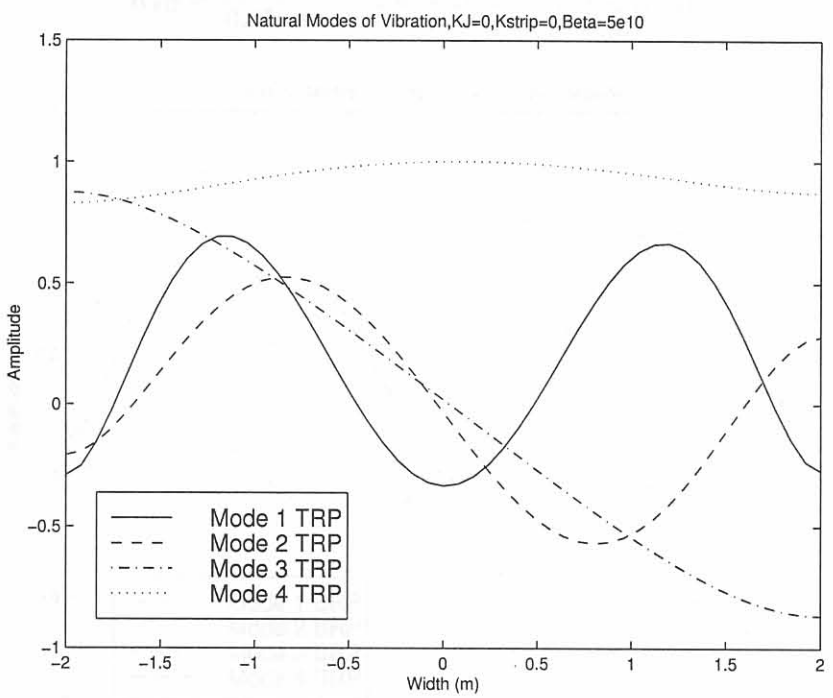

Figure 4.9: Natural modes of vibration for 4 assumed modes of Top Roll Pack.

In chapter 3 the weight of the rollers was not taken into consideration when the model was derived. This modelling choice is motivated by comparing (see table 4.5) the roller weight to the maximum mill rolling force (40MN). From table 4.5 it can be seen that the weight of the roller elements in total is less than 5 % of the maximum rolling force and was thus omitted from the stand model derivation.

Table 4.5: Weight Comparison of Rollers and Chocks against the maximum rolling force, 40MN.

Variable	Weight (kN)	Percentage Value of F_{limit}
Top Work Roll+Chocks+Bearings	179.52	0.449
Bottom Work Roll+Chocks+Bearings	194.24	0.486
Top Back-up Roll+Chocks	762.24	1.91
Bottom Back-up Roll+Chocks	762.24	1.91

Load cells

The discrete spring at the bottom of the mill represents the load cell. The displacement of this hard spring models the load cell behaviour and its compression reflects the rolling force in the mill. It was decided to model this spring according to an ABB Stainless Steel load cell used in the industry for roll force measurement in hot rolling mills. The rectangular load cell, type PFVL 101V, of the Millmate Roll Force System range was chosen [77]. The spring compression at nominal load is not to exceed 0.05mm and if nominal load is taken as half the mill force limit on either side of the mill, the spring constant is found to be,

$$K_{sB} = \frac{0.5F_{limit}}{0.05mm} = 400 \times 10^9 N/m, \forall s \in [L, R]. \tag{4.61}$$

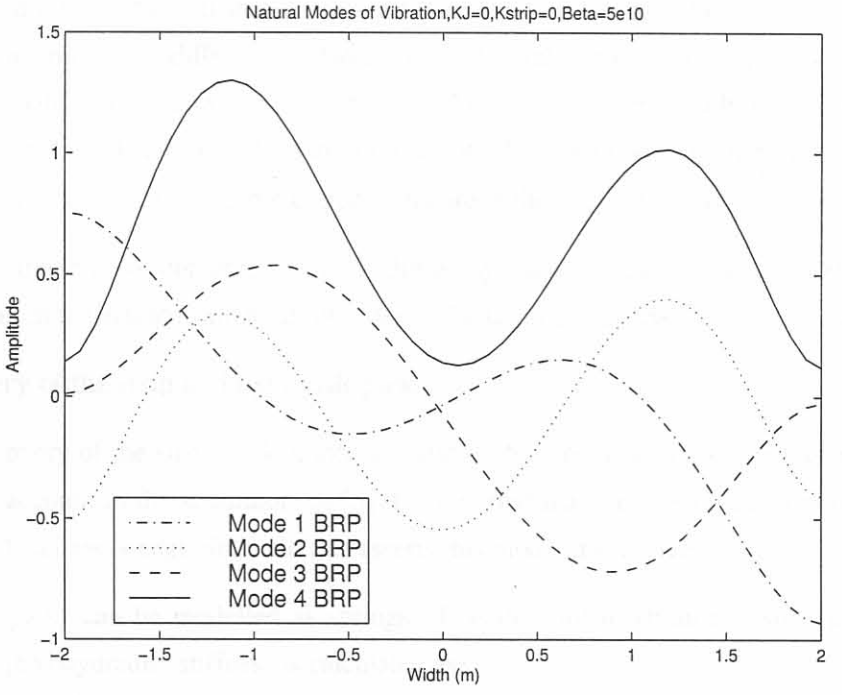

Figure 4.10: Natural modes of vibration for 4 assumed modes of Bottom Roll Pack.

Damping

In [8] damping for the HAGC system is provided between the strip and the working rolls. It is reported in [78] that this damping is dependent on the length of the arc of contact in the roll gap. R-M Guo showed in [8] that there is a contradiction with the statements in [78] and practical data obtained in [8]. In the absence of a correction to this damping equation defined in [78], the same equation will be used namely,

$$\beta_{strip}(t).w = \frac{w.k(\epsilon,\dot{\epsilon},\theta)|_{x_{rg}=0}}{\omega_{main}(t)} \left[\frac{N}{m.s^{-1}}\right], \tag{4.62}$$

where $k(\epsilon,\dot{\epsilon},\theta)|_{x_{rg}=0}$ ($\approx 280MPa$) is the yield stress of the material at the delivery side of the roll gap, $\omega_{main}(t)$ is the main mill drive angular velocity and w is the strip width (1.4m). From the logged data, concentrating only on the similarly identified strips, damping coefficients for pass 1, $\beta_{strip}|_{pass1} = 1.48 \times 10^8$, and pass 3, $\beta_{strip}|_{pass3} = 1.18 \times 10^8 N.m^{-1}.s$, were calculated. However with these damping coefficients a non-bumpless start of the simulation from the chosen steady state resulted. In chapter 5 section 5.3.2, simulation results for a $\beta_{strip}|_{pass3} = 1 \times 10^8 N.m^{-1}.s$ are compared to other values for the distributed friction coefficient.

The nearly steady state point could be maintained by increasing β_{strip}. The general observation was that the mill oscillation could not completely be damped out. Time simulations in [40] also exhibited such oscillatory behaviour and in this investigation [40] damping was only modelled between the strip and the work rolls. In chapter 5 damping ratios for the mill stand model with different β_{strip} and K_J are shown and discussed. An investigation of the damping found in the mill stand might prove beneficiary for the long term research program.

From the logged data of the exit thickness (see figure 4.2) it is not possible to draw conclusions of these oscillations, due to the difference between the high oscillation period frequency, when $\beta_{strip} = 5e10N.m^{-1}.s$, with an oscillating period of roughly 2.6ms and the time resolution of the logged data is 0.4 seconds. The oscillation periods of the 3 modes of vibration in [40] fall in the range of 3ms-4ms. The amplitude of oscillation is not that extreme and are in the order of $2\mu m$.

It needs to be stressed that damping in the nonlinear hydraulic actuator was not modelled and that maybe damping in the actuator might absorb these vibration oscillations.

Elastic recovery of the strip and hydraulic jacks

The elastic recovery of the strip is taken into account in the model derivation, but as a first iteration not taken into account in the simulator. In [3] it is reported that the elastic recovery of the strip for hot rolling applications is negligible and this asserts this modelling choice.

The hydraulic jacks can be modelled as springs. It is difficult to attain realistic values for these springs, but in [65] hydraulic stiffness is calculated as,

$$K_J = \frac{A\beta_o}{h_2}, \tag{4.63}$$

where A is the working area of the actuator, $\beta_o = 1.38GPa$ is the oil's bulk modulus and $\overline{h_2}$ is the average exit thickness of the roll gap assuming the hydraulic jacks coincide on the same vertical yz plane as the exit from the roll gap. The actuator working area is calculated by taking the four bending cylinders per bending block, of which 2 bending blocks per mill side are fitted. A bending cylinder has a full bore side diameter of 210mm. Using Eq. 4.63, the hydraulic stiffness is calculated as $K_J|_{pass3} \approx 40 \times 10^9 N/m$.

It is found that using this magnitude for the bending stiffness coupled the upper and lower roll packs to such an extent that the first natural mode of vibration was dominant for both roll packs. The vibration behaviour of the lower roll pack should be dominated by the second spatial mode of vibration, according to the results obtained by Pederson [59]. This roll pack should only exhibit an increasing/decreasing amount of bending as the rolling force increases/decreases. The displacements at the end of the roll pack should reflect these force deviations by increasing the compression of the load cell spring or reducing it respectively. Taking this statement into consideration and the fact that the elastic recovery of the strip is limited, the upper and lower roll packs are completely decoupled by making $k_{strip} = 0$ and $K_{Js} = 0, \forall s \in [L, R]$.

In figures 4.11 and 4.12 the effect of the jack springs are compared according to the natural modes of vibrations obtained. When the jack springs are large the asymmetrical behaviour between upper and lower roll packs are accentuated in figure 4.12 when compared to 4.11.

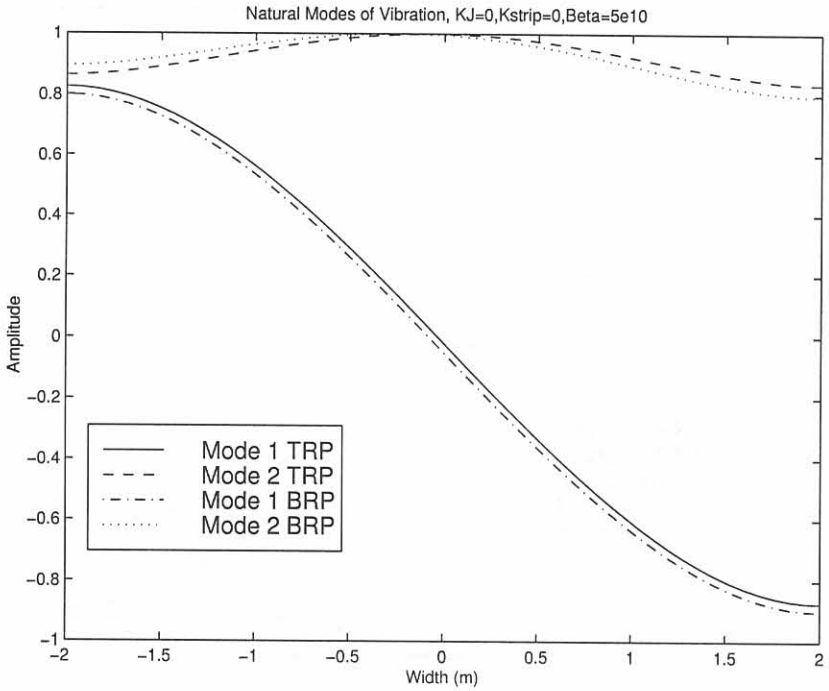

Figure 4.11: Natural modes of vibration for $K_{Js} = 0$ and $\beta_{strip} = 5 \times 10^{10} N.m^{-1}.s$.

4.5.4 Mill Stretch Model

Tests are conducted by plant personnel on the mill under study in order to calculate the mill spring curves for either side of the rolling mill. The test conducted on the mill can be described as follows:

The top roll pack is placed in contact with the bottom roll pack, without a strip in the roll gap. Once the rollers are in place the top roll pack is pressed against the roll pack with a measured force, $F_{test_s} \approx 730Tons$, and at this force level the initial mill stretch $y_{stretch_{test_s}}$ (where $s \in [L, R]$) is logged. The force is then increased until a total rolling force of roughly 30MN is measured (15MN per side). The mill stretch curves (see figure 3.4) are calculated using the values shown in table 4.6.

In [65] the structural stiffness of a rolling mill is given as $16.65 \times 10^6 lb/in = 2.93 \times 10^9 N/m$ and in [59] the structural stiffness of the investigated plate mill is $2.02 \times 10^9 N/m$. These values are in accordance with the calculated values (see table 4.6) for the Steckel Mill under consideration.

Table 4.6: Mill stretch model values

Side	F_{test_s} (MN)	$y_{stretch_{test_s}}$ (mm)	K_{sT} (N/m)
$s = L$ (OS)	7.217	2.774	3.388×10^9
$s = R$ (DS)	7.190	2.765	3.413×10^9

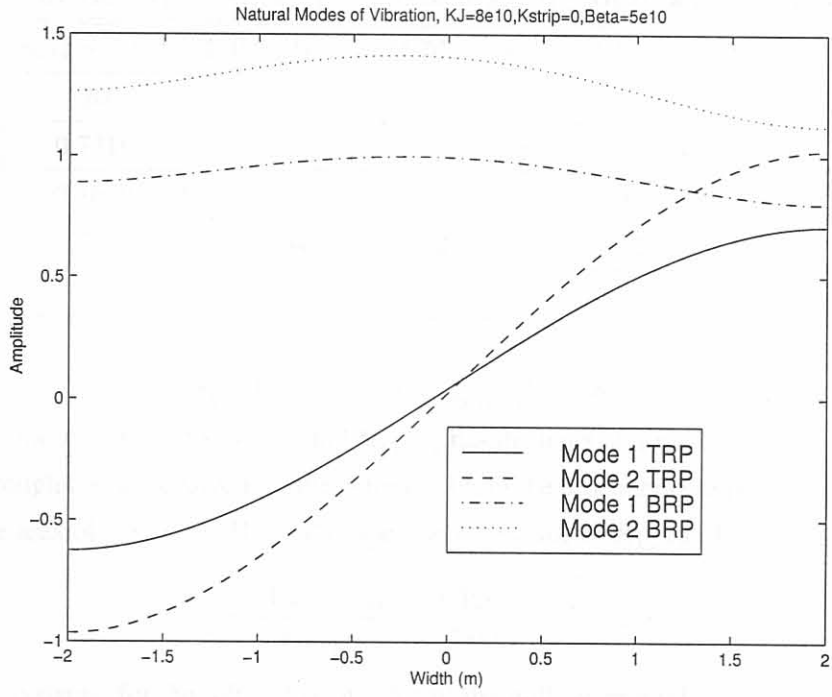

Figure 4.12: Natural modes of vibration for $K_{Js} = 80 \times 10^9 N/m$ and $\beta_{strip} = 5 \times 10^{10} N.m^{-1}.s$.

4.6 Hydraulic actuator model

Data of the implemented plant actuators for the Steckel mill under consideration are not available. Information of the physical constants and dimensions of such actuators had to be extracted from articles [8, 64, 65, 79] and a servovalve manufacturer brochure [68]. This procedure was deemed necessary in order to get a true reflection of the physical system.

4.6.1 Physical constants

Different types of servovalves are used in the rolling mill environment. The Steckel Mill, under investigation, uses a servovalve with a natural frequency, f_s, of 51Hz[16]. This value agrees with the operating frequency range for servovalves, 60 - 100 Hz, listed by Guo [8]. Using this specified frequency range as a criteria, the Moog Servovalve D661-range was identified from [68].

Table 4.7 relates values for different hydraulic systems found in the literature as well as values of the D661 servovalve. All the listed values were converted into SI Units in order to compare them and to motivate choices for the simulator.

Table 4.7: Comparison of hydraulic system parameters.

Variable	Bhowal [64]	Guo [8]	Ginzburg [65]	Huzyak [79]	Moog D661 [68]
q_0 ($\frac{m^3}{s}$)	6.67×10^{-4}	1.45×10^{-3}	4.70×10^{-3}	1.58×10^{-3}	1.33×10^{-3}
I_0 (mA)	20	-	30	20	10
A_1 (m^2)	0.7310	-	0.6243 m^2	0.6243	-
A_2 (m^2)	0.1639	-	-	0.1698	-
P_s (MPa)	25	31.04	27.59	27.59	35
P_t (MPa)	6	-	-	-	5

Cylinder flow is calculated using, $Q = A\vartheta = K_{v_s} x_{v_s} \sqrt{\frac{\Delta P}{\rho}}$, where the term incorporating the pressure difference has the units of velocity, and $K_{v_s} x_{v_s}$ has the units of area. The rated flow of the valve has to pass through the servovalve into the cylinder. From the brochure data [68] this area is taken as the spool drive area of 1.35 cm^2. Using this approach the value of K_{v_s} can be calculated as,

$$K_{v_s} = \frac{A_{spool\ drive}}{x_{v_s max}} = \frac{1.35cm^2}{3mm} = 0.045m.$$

The hydraulic systems, for the left and right sides of the mill, were modelled using the values summarized in Table 4.8.

It is assumed that the response of the second order transfer function servovalve model is critically damped. This assumption can be motivated by referring to time response curves [68]. Once the spool

[16]Personal correspondence with M. Lewis.

movement is larger than 100% the flow, associated with a certain pressure drop, can not exceed the maximum flow, and a stroke greater than 100% will not reflect this limitation. This phenomena was incorporated as a hard constraint on the stroke length of $\pm 3mm$ in the mill simulator.

The thrust force capability of the modelled actuators are given in table 4.9, and a physical constraint of 40MN (20MN on each side of the mill) is applied. The modelled actuators are therefore capable of handling these large rolling forces (20MN).

4.7 Dynamic Simulator

The dynamic simulator consists of two dynamic models. The two models are the tension model and a combination of the hydraulic actuator models and the stand model. The tension model is simulated at a higher sampling rate than the rest of the simulator. The combination of the hydraulic actuator models and the stand model is expressed as a non linear state-space model. This nonlinear state-space

Table 4.8: Hydraulic Model System Parameters

Variable	Value
q_0	$1.5 \times 10^{-3}\ \frac{m^3}{s}$
I_0	± 10 mA
A_1	$0.74\ m^2$
A_2	$0.16\ m^2$
P_{high}	35 MPa
P_{low}	5 MPa
w_v	$2\pi \times 51\ \frac{rad}{s}$
ζ_v	1
K_{leak}	1×10^{-9}
K_{v_s}	0.045 m
$x_{v_{s_{max}}}$	3×10^{-3} m
K_{c_s}	1.5
τ_{i_s}	1×10^{-2}

Table 4.9: Thrust force capability.

P_{s1} (MPa)	P_{s2} (MPa)	F_{HA_s} (MN)
5	5	2.9
5	35	-1.9
35	5	25.1
35	35	20.3

model is solved using a fourth order fixed time step Runge Kutta method [71].

The spatial modelling of the rollers provides the simulator with the draft deviation across the width of the sheet. This deviation is used to solve the roll gap model at some of the 51 discretized nodes in order to yield varying specific rolling forces across the width of the strip. It is assumed that the strip is very ductile at 1000°C and that the strip does fill the whole roll gap. The simulator is not able to account for strip with an entering negative (concave) crown, because the strip will not fill the whole roll gap along the curvature of bended rolls. In the simulator the spatial dynamic draft is calculated utilizing the following equation,

$$\begin{aligned}\delta(z,t) &= h_{1_{setup}} - h_{2_{setup}} - (\delta h_1(t) - \delta h_2(z,t)) \\ &= \delta_{setup} - (\delta h_1(t) - (y_1(z,t) - y_2(z,t))), \quad where \ \tfrac{-w}{2} \leq z \leq \tfrac{w}{2}.\end{aligned} \tag{4.64}$$

$\delta h_1(t)$ is taken as the measured entrance thickness deviation at the center of the strip. $\delta h_2(z,t)$ is evaluated over the width of the strip.

In figure 4.13 the flow chart of the mill simulator is shown. This high level flow chart shows how the various models are used in the mill simulator.

The nonlinear state-space model of the simulator will be expressed for the two roll pack system with two assumed modes per roller. The assignment of states for the nonlinear state-space model is as follows[17]:

$$\mathbf{x} = \begin{bmatrix} \mathbf{x}_a & \mathbf{x}_b \end{bmatrix}^T, \tag{4.65}$$

$$\mathbf{x}_a = \begin{bmatrix} x_1 & x_2 & x_3 & x_4 & x_5 & x_6 & x_7 & x_8 \end{bmatrix}^T = \begin{bmatrix} q_{1_1} & q_{1_2} & q_{2_1} & q_{2_2} & \dot{q}_{1_1} & \dot{q}_{1_2} & \dot{q}_{2_1} & \dot{q}_{2_2} \end{bmatrix}^T, \tag{4.66}$$

where $q_{i_j}, \forall i,j \in [1,2]$ were defined in section 4.5.2.4.

The state assignments associated with the hydraulic actuators are,

$$\begin{aligned}\mathbf{x}_b = &\begin{bmatrix} x_9 & x_{10} & x_{11} & x_{12} & x_{13} & x_{14} & x_{15} & x_{16} & x_{17} & x_{18} \end{bmatrix}^T = \\ &\begin{bmatrix} x_{v_L} & \dot{x}_{v_L} & P_{L1} & x_{v_R} & \dot{x}_{v_R} & P_{R1} & P_{L2} & P_{R2} & x_L & x_R \end{bmatrix}^T,\end{aligned} \tag{4.67}$$

and the input vector of the dynamic simulator is,

$$\mathbf{u} = \begin{bmatrix} x_{11} & x_{15} & x_{14} & x_{16} & P'(z) \end{bmatrix}^T. \tag{4.68}$$

The flows of the hydraulic actuator models expressed as functions of the states are as follows:

$$Q_{L1} = \begin{cases} K_{v_L} x_9 \sqrt{\frac{2}{\rho_o}(P_s - x_{11})}, & when \ x_9 \geq 0 \\ K_{v_L} x_9 \sqrt{\frac{2}{\rho_o}(x_{11} - P_t)}, & when \ x_9 < 0 \end{cases}, \tag{4.69}$$

[17] All of the variables have previously been defined in chapter 3.

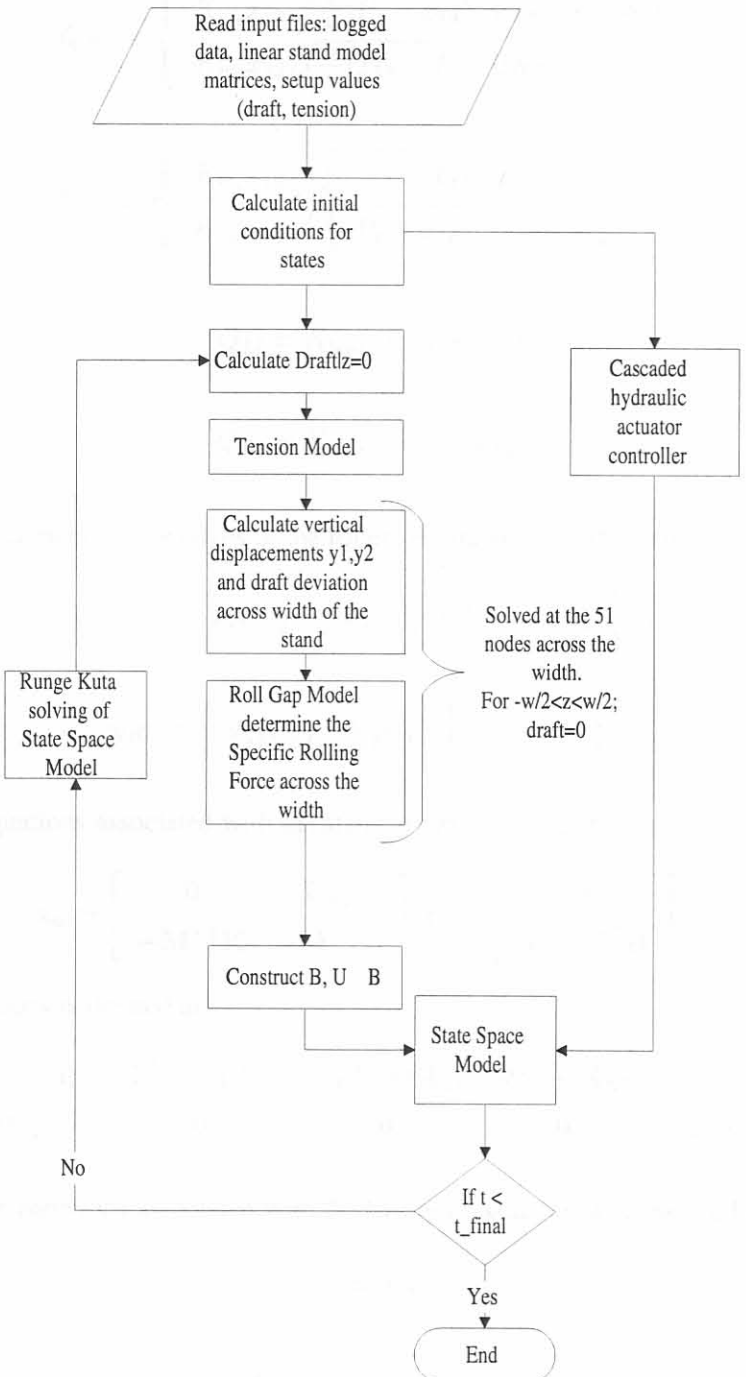

Figure 4.13: Mill simulator flowchart

$$Q_{L2} = \begin{cases} K_{v_L} x_9 \sqrt{\frac{2}{\rho_o}(x_{15} - P_t)}, & when\ x_9 \geq 0 \\ K_{v_L} x_9 \sqrt{\frac{2}{\rho_o}(P_s - x_{15})}, & when\ x_9 < 0 \end{cases}, \tag{4.70}$$

$$Q_{R1} = \begin{cases} K_{v_R} x_{12} \sqrt{\frac{2}{\rho_o}(P_s - x_{14})}, & when\ x_{12} \geq 0 \\ K_{v_R} x_{12} \sqrt{\frac{2}{\rho_o}(x_{14} - P_t)}, & when\ x_{12} < 0 \end{cases}, \tag{4.71}$$

$$Q_{R2} = \begin{cases} K_{v_R} x_{12} \sqrt{\frac{2}{\rho_o}(x_{16} - P_t)}, & when\ x_{12} \geq 0 \\ K_{v_R} x_{12} \sqrt{\frac{2}{\rho_o}(P_s - x_{16})}, & when\ x_{12} < 0 \end{cases}, \tag{4.72}$$

$$Q_{Ll} = K_{leak_L}(x_{11} - x_{15}), \tag{4.73}$$

$$Q_{Rl} = K_{leak_R}(x_{14} - x_{16}), \tag{4.74}$$

The vertical displacements at the edges of the rollers as functions of the states are,

$$y_{LT} = \begin{bmatrix} \phi_{1_1}(\frac{-l_1}{2}) & \phi_{1_2}(\frac{-l_1}{2}) \end{bmatrix} \begin{bmatrix} x_1 & x_2 \end{bmatrix}^T; \tag{4.75}$$

$$y_{RT} = \begin{bmatrix} \phi_{1_1}(\frac{l_1}{2}) & \phi_{1_2}(\frac{l_1}{2}) \end{bmatrix} \begin{bmatrix} x_1 & x_2 \end{bmatrix}^T; \tag{4.76}$$

The linear state equations associated with the stand are expressed as follows,

$$\dot{\mathbf{x}}_a = \begin{bmatrix} \mathbf{0} & \mathbf{I}_{2\times 2} \\ -\mathbf{M}^{-1}\mathbf{K} & -\mathbf{M}^{-1}\mathbf{C} \end{bmatrix} \mathbf{x}_a + \begin{bmatrix} \mathbf{0} \\ \mathbf{M}^{-1}\mathbf{U}^{\mathbf{T}}\mathbf{B} \end{bmatrix} \mathbf{u}, \tag{4.77}$$

where the input matrix is defined as,

$$\mathbf{B} = \begin{bmatrix} -\Psi_1^T(\frac{-l_1}{2})A_{L1} & \Psi_1^T(\frac{-l_1}{2})A_{L2} & -\Psi_1^T(\frac{l_1}{2})A_{R1} & \Psi_1^T(\frac{l_1}{2})A_{R2} & \Delta_z\Psi_1(z)^T \\ \mathbf{0} & \mathbf{0} & \mathbf{0} & \mathbf{0} & -\Delta_z\Psi_2(z)^T \end{bmatrix}. \tag{4.78}$$

The nonlinear state equations associated with the hydraulic systems are expressed as,

$$\dot{x}_9 = x_{10}, \tag{4.79}$$

$$\dot{x}_{10} = -2\zeta_{v_L}\omega_{v_L}x_{10} - \omega_{v_L}^2 x_9 + \omega_{v_L}^2 I_{c_L}, \tag{4.80}$$

$$\dot{x}_{11} = \frac{Q_{L1} - Q_{Ll} + A_{L1}\dot{y}_{L1} - \frac{A_{L1}A_{L2}}{K_{LT}\Delta}(Q_{L2} - Q_{Ll} + A_{L2}\dot{y}_{LT})}{\frac{V_{L1}(x_{17})}{\beta_o} + \frac{A_{L1}^2}{K_{LT}} - \frac{(A_{L1}A_{L2})^2}{K_{LT}^2\Delta}}, \tag{4.81}$$

$$\dot{x}_{12} = x_{13}, \tag{4.82}$$

$$\dot{x}_{13} = -2\zeta_{v_L}\omega_{v_L}x_{13} - \omega_{v_L}^2 x_{12} + \omega_{v_L}^2 I_{c_R}, \tag{4.83}$$

$$\dot{x}_{14} = \frac{Q_{R1} - Q_{Rl} + A_{R1}\dot{y}_{R1} - \frac{A_{s1}A_{s2}}{K_{sT}\Delta}\left(Q_{R2} - Q_{Rl} + A_{R2}\dot{y}_{RT}\right)}{\frac{V_{R1}}{\beta_o} + \frac{A_{R1}^2}{K_{RT}} - \frac{(A_{R1}A_{R2})^2}{K_{RT}^2\Delta}}, \tag{4.84}$$

$$\dot{x}_{15} = \frac{-Q_{L2} + Q_{Ll} - A_{L2}\dot{y}_{LT} + \frac{x_{11}A_{L1}A_{L2}}{K_{LT}}}{\left(\frac{V_{L2}}{\beta_o} + \frac{A_{L2}^2}{K_{LT}}\right)}, \tag{4.85}$$

$$\dot{x}_{16} = \frac{-Q_{R2} + Q_{Rl} - A_{R2}\dot{y}_{RT} + \frac{x_{14}A_{R1}A_{R2}}{K_{RT}}}{\left(\frac{V_{R2}}{\beta_o} + \frac{A_{R2}^2}{K_{RT}}\right)}, \tag{4.86}$$

$$\dot{x}_{17} = \frac{\dot{x}_{11}A_{L1} - \dot{x}_{15}A_{L2}}{K_{LT}} - \dot{y}_{LT}, \tag{4.87}$$

$$\dot{x}_{18} = \frac{\dot{x}_{14}A_{R1} - \dot{x}_{16}A_{R2}}{K_{RT}} - \dot{y}_{RT}, \tag{4.88}$$

It needs to be stressed that most of these states are not defined as small signal variables and reflect total state values for some state variables. The states associated with the linear stand model are expressed as small signal deviation state values. The states associated with the hydraulic actuators are not expressed as small signal state variables.

4.8 Conclusion

In this chapter the solution methodologies for each of the models identified in chapter 3 were discussed. These models were incorporated into a mill simulator and the chapter ended with the expression of the nonlinear state space model associated with the hydraulic actuator and stand model combination. The tension model can not operate independently and uses the roll gap model in order to solve the implicit relationship between the tensions and the roll gap speeds as well as the time advancement of the tension simulation. The tension model is solved at a specific time instance using the draft value at the middle of the strip. These tension values are used in the solution process of the nonlinear state-space model of the stand and actuators combination. In the following chapter, simulation results and the system identification for control purposes will be shown.